Supporting Information

-for-

High-Entropy $Cr(NiFeCoV)_2O_4$ Catalysts via CO_2 Laser Thermal Shock: Advancing Electrochemical Water Oxidation with Multi-Metal Synergy

*Sharanya Kannan Anbarasu [a,†], Raja Arumugam Senthil [a,†], Sieon Jung [a], Anuj Kumar [b], Mohd Ubaidullah [c], Myong Yong Choi [a,d,]**

[a] *Department of Chemistry (BK21 FOUR), Research Institute of Advanced Chemistry, Gyeongsang National University, Jinju 52828, Republic of Korea*

[b] *Nano-Technology Research Laboratory, Department of Chemistry, GLA University, Mathura, Uttar Pradesh 281406, India*

[c] *Department of Chemistry, College of Science, King Saud University, Riyadh 11451, Saudi Arabia*

[d] *Core-Facility Center for Photochemistry & Nanomaterials, Gyeongsang National University, Jinju 52828, Republic of Korea*

* Corresponding author E-mail address: mychoi@gnu.ac.kr (M.Y. Choi)

† These authors contributed equally to this work

Characterization Analyses

The synthesized electrocatalysts were extensively analyzed using various advanced techniques to explore their structural formation, surface morphology, elemental composition, and chemical properties. The surface topography and elemental mapping were checked through field emission scanning electron microscopy (FESEM, TESCAN S-8000, Czech Republic) coupled with energy-dispersive X-ray spectroscopy (EDS, Ultim Max, Oxford). High-resolution transmission electron microscopy (HR-TEM, Talos F200X, FEI Company, USA) was employed to provide detailed insights into the nanoscale structural features of the materilas. The crystalline structure and phase purity of the electrocatalysts were confirmed through X-ray diffraction (XRD) analysis, performed on a Bruker D8 Advance A25 X-ray diffractometer (Germany) using a Cu–Kα radiation (λ = 0.154 nm). Raman spectroscopy was conducted with a DXR3 Raman microscope (Thermo Fisher Scientific, USA) equipped with a 532 nm Nd:YAG laser as the excitation source, to analyze vibrational characteristics. Fourier-transform infrared spectroscopy (FTIR) measurements were performed on a Nicolet iS10 spectrometer (Thermo Fisher Scientific, USA) to identify functional groups present in the electrocatalysts. X-ray photoelectron spectroscopy (XPS, NEXSA G2, Thermo Fisher Scientific, USA) with monochromatic Al–Kα radiation was utilized to determine the oxidation states of metals, bonding environments, and surface elemental composition. Additionally, the specific surface area of the electrocatalysts was measured using the Brunauer Emmett Teller (BET) method with a BELSORP-mini II surface area analyzer (BEL Japan, Inc., Japan).

Fabrication of the Working Electrode

To fabricate the working electrode, 1 mg of the synthesized catalyst was dispersed in a solution comprising 180 µL of isopropanol and 20 µL of 5 wt% Nafion binder. The resulting mixture was sonicated for 30 nm to achieve a homogeneous suspension. The prepared catalyst ink was uniformly coated onto a pre-treated nickel foam (NF) substrate with dimensions of 1 × 1 cm^2 and subsequently dried at 80°C for 3 h.

Electrochemical Measurements

The electrocatalytic performance of the HE-$Cr(NiFeCoV)_2O_4$ catalyst for OER was evaluated using a CHI 708E electrochemical workstation (CH Instruments Inc, USA). A standard three-electrode setup was employed, consisting of the catalyst-loaded NF substrate as the working electrode, a graphite rod as the counter electrode, and a Hg/HgO electrode as the reference electrode. All electrochemical measurements were conducted in 1 M KOH as the electrolyte. The potentials recorded against the Hg/HgO reference electrode were converted to the reversible hydrogen electrode (RHE) scale using Equation (1):

$$E_{RHE} = E_{Hg/HgO} + E^{0}_{Hg/HgO} + 0.059\ V \times pH \quad (1)$$

where $E_{Hg/HgO}$ is the measured potential, $E^{0}_{Hg/HgO}$ is the standard electrode potential (0.098 V), and pH is the pH of the electrolyte.

The Tafel slope, a key parameter for assessing reaction kinetics, was derived from the relationship between the overpotential (η) and current density (j), as expressed in Equation (2):

$$\eta = b \times \log(j) + a \quad (2)$$

where b is the Tafel slope and a is the Tafel constant.

Mass activity and turnover frequency (TOF) were calculated to evaluate the intrinsic catalytic activity of the electrocatalysts. The mass activity ($A \cdot g^{-1}$) of the electrocatalysts was calculated using Equation (3):

$$\text{Mass activity} = \frac{j}{m} \quad (3)$$

where, j indicates the current density and m denotes the catalyst mass.

Additionally, the turnover frequency (TOF) of the electrocatalysts was estimated using Equation (4):

$$\text{TOF } (s^{-1}) = \frac{j \, x \, N_A}{n \, x \, F \, x \, S_a} \quad (4)$$

where N_A is Avogadro's number, n is the number of electrons transferred in the reaction (which is 4 for OER), F is the Faraday constant (96,485.3 C mol^{-1}), and S_a is the number of active sites. The active sites (S_a) was assessed using Equation (5):

$$S_a = \frac{(\int Area\ under\ the\ reduction\ curve / Scan\ rate)}{Charge\ of\ the\ electron} \quad (5)$$

Electrochemical impedance spectroscopy (EIS) was conducted to analyze the charge transfer resistance (R_{ct}), with Nyquist plots were generated over a frequency range of 0.1 Hz to 10^5 Hz at a fixed potential (V vs. RHE). The double-layer capacitance (C_{dl}) was assessed by analyzing the difference in anodic and cathodic current densities ($\Delta j/2 = (j_a - j_c)/2$) at varying scan rates. The slope of the linear plot yielded C_{dl} as per Equation (6):

$$C_{dl} = \frac{d(\Delta j)}{2dv} \quad (6)$$

where ν is the scan rate.

Subsequently, the electrochemical surface area (ECSA) was determined via Equation (7):

$$\text{ECSA} = \frac{C_{dl}}{C_s} \quad (7)$$

Where C_s is the specific capacitance of NF substrate.

In situ Raman Spectroscopy Analysis

In situ Raman spectroscopy was conducted using a custom-built electrochemical cell (redoxme AB, Sweden) configured with a three-electrode system. This setup comprised a catalyst-loaded NF substrate as the working electrode, a graphite wire as the counter electrode, and a Hg/HgO referencd electrode. All measurements were performed in a 1 M KOH electrolyte using a CHI 708E electrochemical workstation (CH Instruments Inc., USA). A DXR3 Raman spectrometer (Thermo Fisher Scientific, England) equipped with a 532 nm Nd:YAG laser and a high resolution 50× objective beam lens was employed to collect Raman spectra. This system enabled the monitoring of real-time spectral changes under varying applied potentials during the OER. The *in situ* Raman spectra provided direct insights into surface intermediates and structural transformations occurring on the catalyst during OER operation, revealing the dynamic evolution of active species and their interaction with the catalyst's surface under electrochemical conditions.

Theoretical Simulation Details

To construct the high-entropy HE-Cr(NiFeCoV)$_2$O$_4$ (HE-Cr(NiFeCoV)$_2$O$_4$) model, we adopted the following strategy. An equimolar ratio of Cr, Co, Ni, Fe, and V elements was used, with Ni, Fe, and V systematically introduced into the spinel $CrCo_2O_4$ structure, maintaining its

structural consistency. In the $CrCo_2O_4$, Cr^{3+} and Co^{2+} ions occupy the tetrahedral and octahedral sites, respectively. For the HE-$Cr(NiFeCoV)_2O_4$ configuration, the spinel framework was retained, wherein Cr^{3+} ions remained in the tetrahedral sites, while Ni^{2+}, Fe^{2+}/Fe^{3+}, Co^{2+}, and V^{3+} ions were randomly distributed across both octahedral and tetrahedral sites depending on their ionic radii and oxidation states. This random distribution resulted in atomic-scale disorder and site occupancy variation, thereby stabilizing a high-entropy phase. The formation energy for each configuration was computed using the following equation (8):

$$E_{formation} = E_{Total} - \left(\eta_{Cr}E_{Cr} + \eta_{Ni}E_{Ni} + \eta_{Fe}E_{Fe} + \eta_{Co}E_{Co} + \eta_{V}E_{V}\right) \quad (8)$$

Where, E_{Total} is the total energy of the HE-$Cr(NiFeCoV)_2O_4$ system, η element is the number of each element in the HE-$Cr(NiFeCoV)_2O_4$ systems, and $E_{element}$ is the energy of pure element.

The HE-$Cr(NiFeCoV)_2O_4$ structure exhibited a lower formation energy of –13.3 eV per formula unit, which is slightly lower than that of the $CrCo_2O_4$ structure (–12.7 eV per formula unit), indicating enhanced stability. A 2×2×2 supercell was used in the calculations. For clarity in atomic visualization, three layers were initially removed in earlier figures; however, the full slab has now been included in the revised manuscript. For all further calculations, including the binding energy of OER intermediates, the (111) crystallographic plane was selected. This is the most thermodynamically stable surface for spinel structures due to its dense atomic packing, which reduces surface energy. Moreover, this plane contains a mix of tetrahedral and octahedral sites, effectively representing the complexity and site disorder of the high-entropy phase.

Density Functional Theory (DFT) calculations were performed using the Quantum ESPRESSO simulation package, which employs plane-wave pseudopotential methods to model electronic structures and catalytic activity. The simulations were focused on the HE-$Cr(NiFeCoV)_2O_4$ catalyst, emphasizing its electronic properties, such as the total density of states

(TDOS), projected density of states (PDOS), charge density distribution, and its electrocatalytic behavior towards OER. The structure was modeled in its spinel phase. All atomic positions were relaxed until the forces acting on atoms were below 0.02 eV/Å. Initial lattice parameters were taken from experimental data, and structural optimization included relaxation of both lattice volume and atomic positions. Ultrasoft pseudopotentials were employed for Cr, Ni, Fe, Co, V, and O to capture their electronic behavior accurately. A plane-wave basis set was used with a kinetic energy cutoff of 50 Ry for wavefunctions and 450 Ry for charge density. Monkhorst-Pack k-point sampling was set to 10×8×6, and the self-consistent field (SCF) convergence threshold was 10^{-6} eV. Convergence tests were also conducted for plane-wave cutoff, k-point density, and vacuum thickness in the slab models. Electronic structure analyses included spin-polarized TDOS and PDOS calculations to determine the contributions from individual atomic orbitals (Cr, Ni, Fe, Co, V, and O). The charge density distribution was examined to understand electron localization and charge transfer processes within the spinel lattice. Visualization of these results was performed using VESTA, enabling spatial interpretation of charge distribution across the structure. The OER mechanism was studied through its four typical proton-coupled electron transfer steps, as outlined in Equations (9–12). The associated reaction energies (ΔE) and Gibbs free energy changes (ΔG) for each step were calculated using Equations (13–19), providing insight into the catalyst's efficiency and potential rate-limiting steps.

$$H_2O + * \rightarrow *OH + H^+ + e^- \quad (9)$$

$$*OH \rightarrow *O + H^+ + e^- \quad (10)$$

$$H_2O(l) + *O \rightarrow *OOH + H^+ + e^- \quad (11)$$

$$*OOH \rightarrow * + O_2 + H^+ + e^- \quad (12)$$

$$\Delta E(*OH) = E(*OH) - E(*) - [E(H_2O) - 0.5(H_2)] \quad (13)$$

$$\Delta G(1) = \Delta E(OH) + \Delta ZPE - T\Delta S - eU + k_B T\ln 10 \bullet pH \quad (14)$$

$$\Delta E(*O) = E(*O) - E(*) - [E(H_2O) - E(H_2)] \quad (15)$$

$$\Delta G(2) = \Delta E(*O) + \Delta ZPE - T\Delta S - eU + k_B T\ln 10 \bullet pH \quad (16)$$

$$\Delta E(*OOH) = E(*OOH) - E(*) - [2E(H_2O) - 1.5E(H_2)] \quad (17)$$

$$\Delta G(3) = \Delta E(*OOH) + \Delta ZPE - T\Delta S - eU + k_B T\ln 10 \bullet pH \quad (18)$$

$$\Delta G(4) = 4.92 - \Delta G(1) - \Delta G(2) - \Delta G(3) \quad (19)$$

In these expressions, the symbol * represents to the active site, while *OH, *O, and *OOH denote to the intermediates adsorbed at the active site. The parameters ΔE(*OH), ΔE(*O), and ΔE(*OOH) signify the energy differences related to the adsorption of *OH, *O, and *OOH species, respectively. The terms ΔZPE and ΔS designate the zero-point energy correction derived from DFT calculations and the entropy change obtained from vibration frequency analysis at T =298 K, respectively. U represents the electrode potential relative to the reversible hydrogen electrode (RHE). The $k_B T\ln 10 \bullet pH$ is a correction factor set to account for the effect of pH, where k_B is the Boltzmann constant.

In a typical OER, the overall reaction involves four proton-coupled electron transfer steps, with a total energy requirement of 4.92 eV. Ideally, this energy is equally distributed among the four steps, meaning that each step requires 1.23 eV to proceed efficiently. The overpotential (η) is defined as the additional potential beyond the standard electrode potential required to drive the reaction. It serves as a crucial metric for evaluating the catalytic activity of a material. The overpotential can be calculated using Equation (20):

$$\eta = \max \frac{[\Delta G(1), \Delta G(2), \Delta G(3), \Delta G(4)]}{e} - 1.23V \quad (20)$$

Where ΔG is the Gibbs free energy change of each elementary step, and e is the elementary charge.

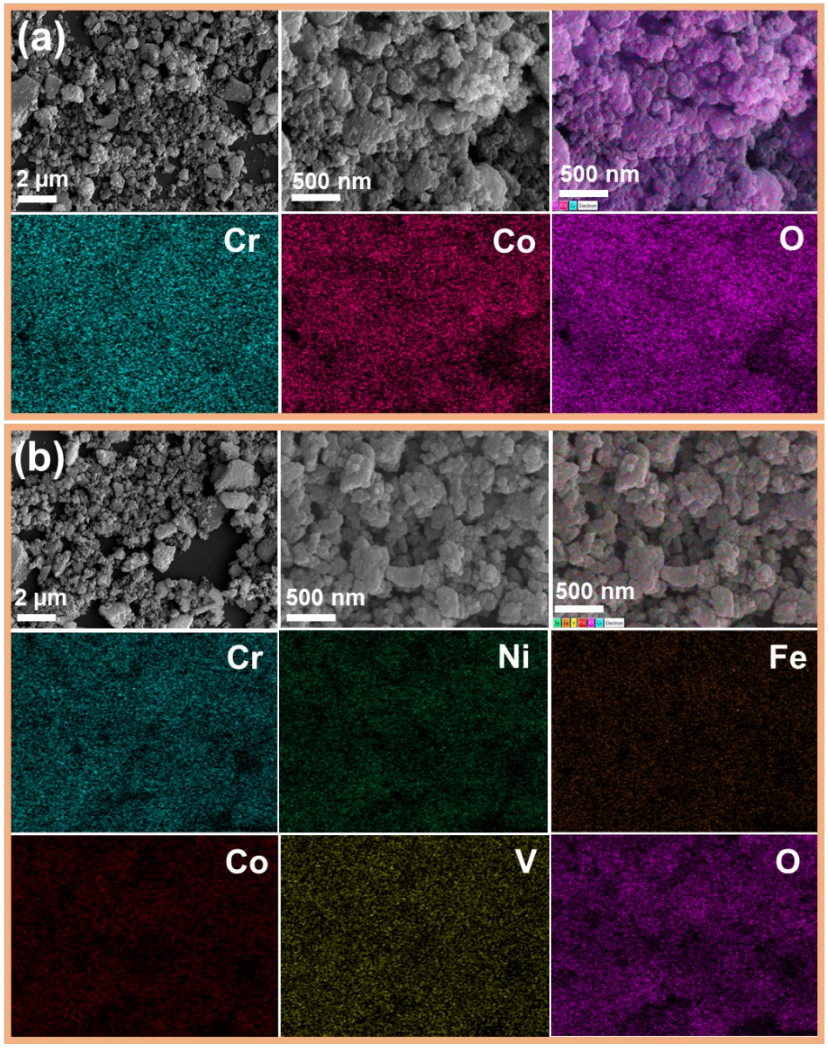

Fig. S1. FESEM and EDS mapping images of (a) $CrCo_2O_4$ and (b) HE-$Cr(NiFeCoV)_2O_4$ catalysts.

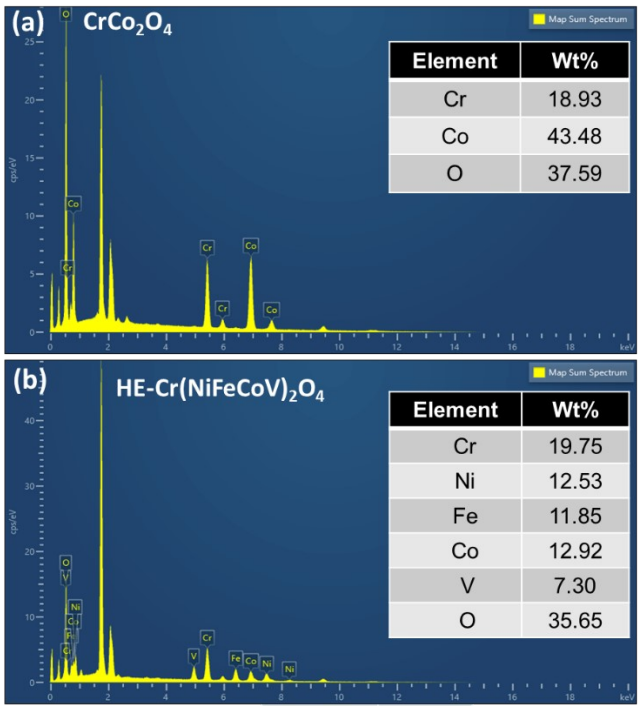

Fig. S2. SEM-EDS spectra of (a) $CrCo_2O_4$ and (b) HE-Cr(NiFeCoV)$_2O_4$ catalysts.

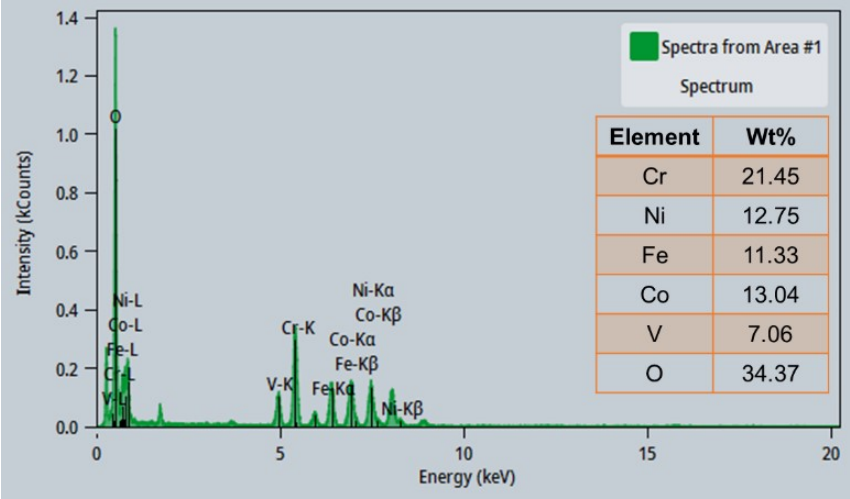

Fig. S3. TEM-EDS spectrum of HE-Cr$(NiFeCoV)_2O_4$ catalyst.

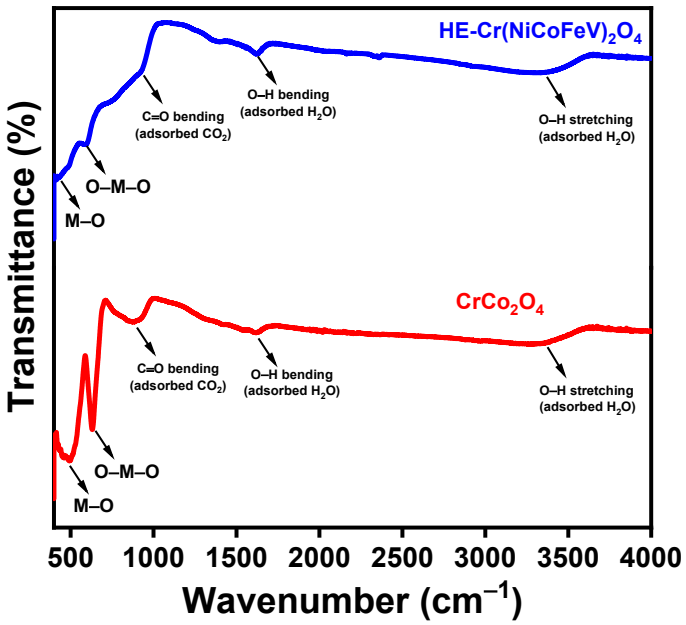

Fig. S4. FTIR spectra of the $CrCo_2O_4$ and HE-$Cr(NiFeCoV)_2O_4$ catalysts.

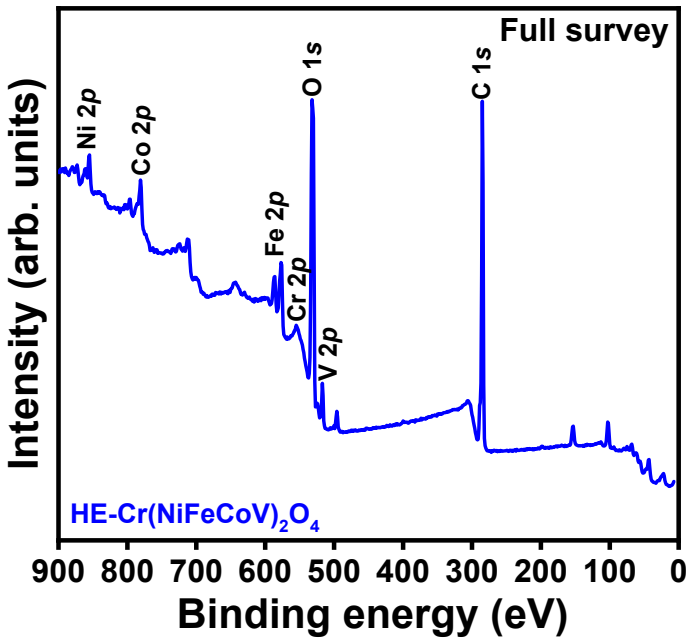

Fig. S5. XPS full survey spectrum of the HE-Cr(NiFeCoV)$_2$O$_4$ catalyst.

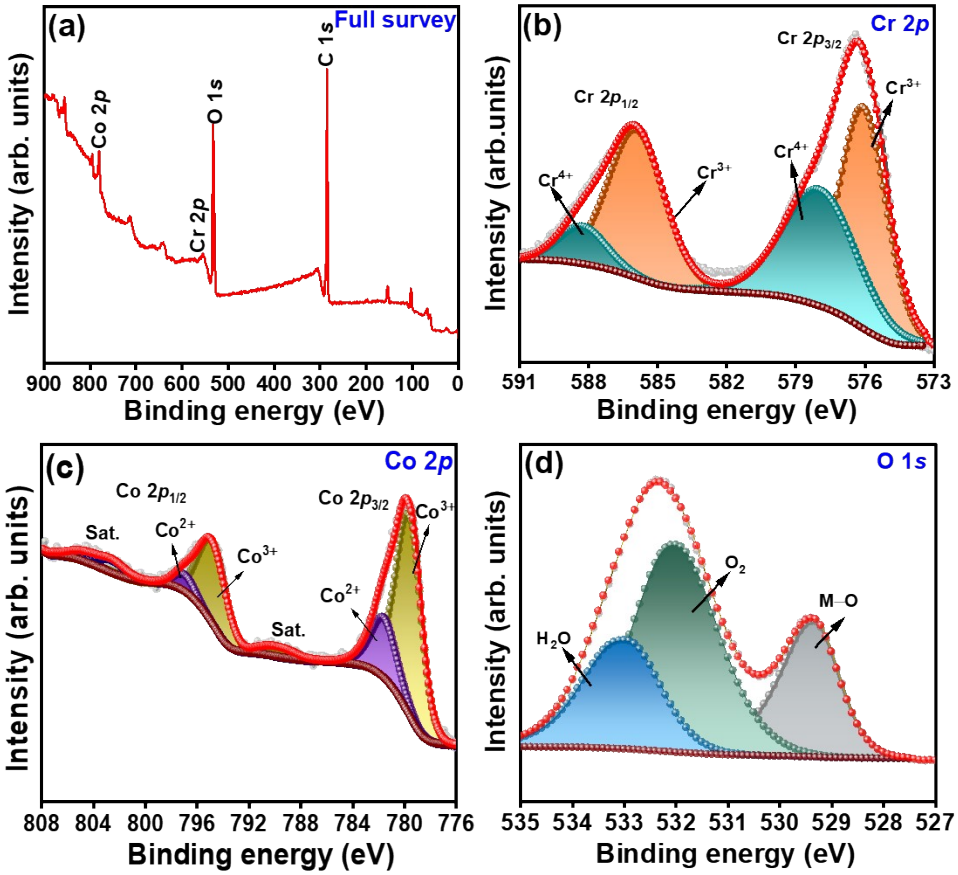

Fig. S6. XPS spectra of the $CrCo_2O_4$ catalyst: (a) Full survey, (b) Cr 2*p*, (c) Co 2*p*, and (d) O1*s*.

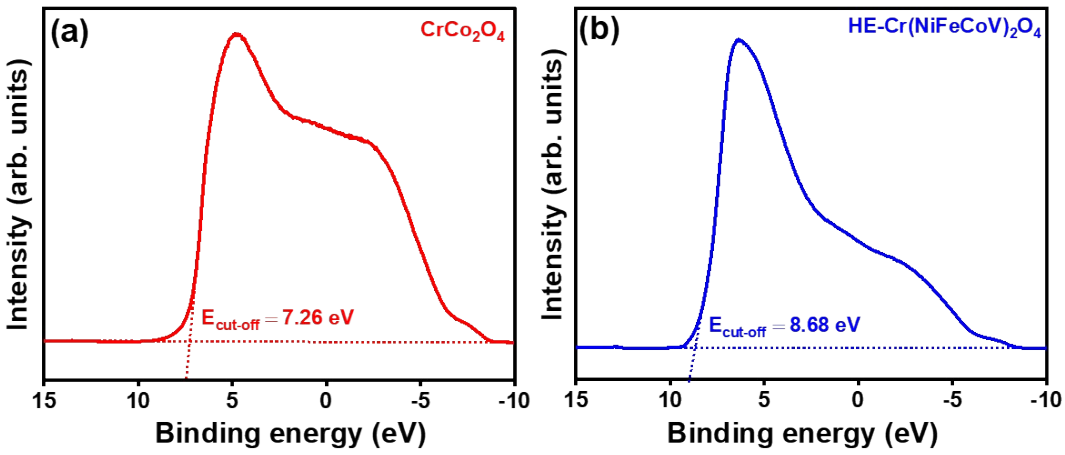

Fig. S7. UPS spectra of (a) $CrCo_2O_4$ and (b) HE-Cr(NiFeCoV)$_2O_4$ catalysts.

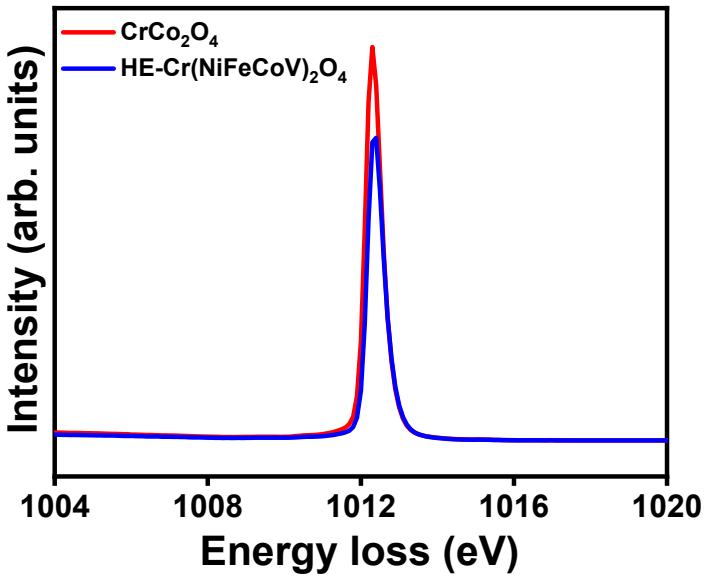

Fig. S8. REELS spectra of the $CrCo_2O_4$ and HE-$Cr(NiFeCoV)_2O_4$ catalysts.

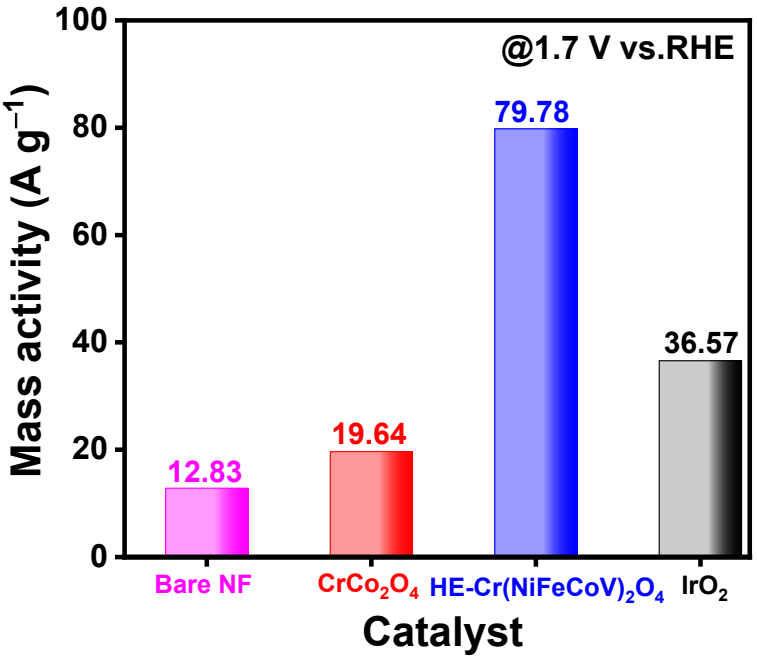

Fig. S9. Mass activity analysis of the bare NF, $CrCo_2O_4$, HE-Cr(NiFeCoV)$_2O_4$, and commercial IrO_2 catalysts for OER.

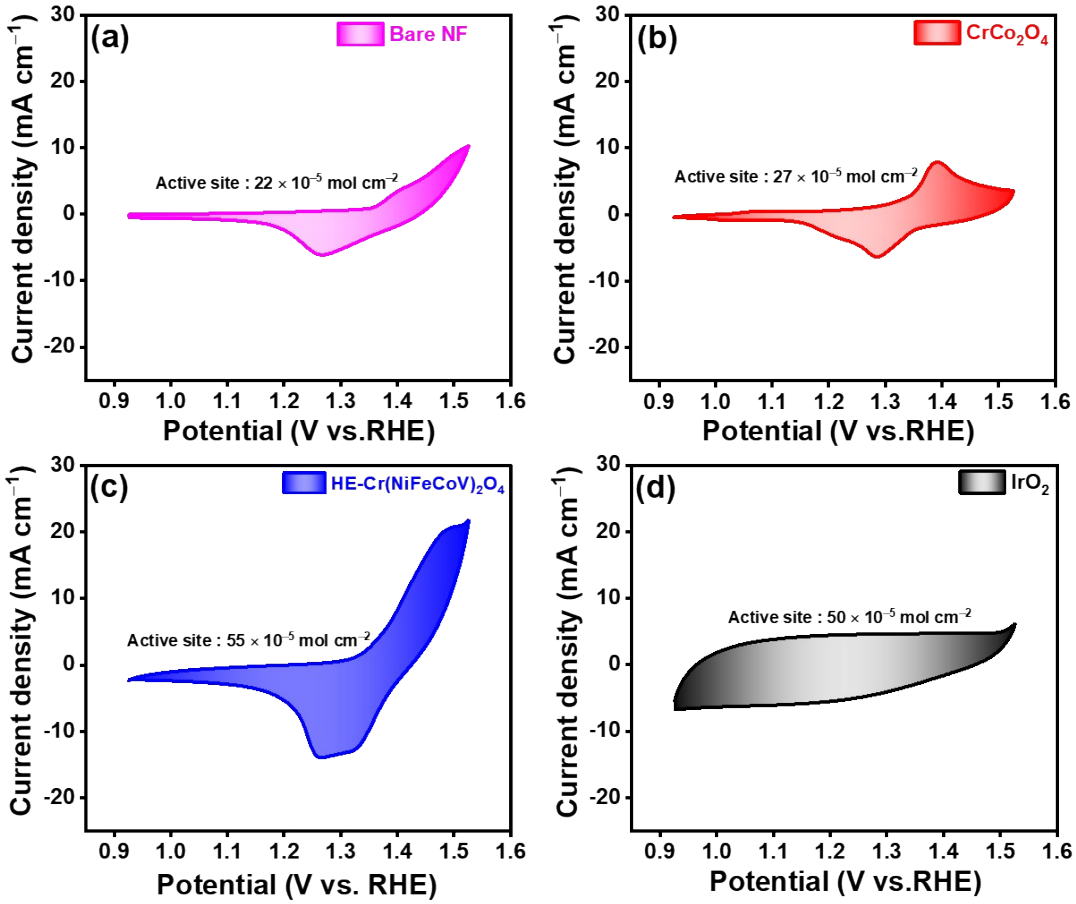

Fig. S10. CV curves of the (a) bare NF, (b) $CrCo_2O_4$, (c) HE-$Cr(NiFeCoV)_2O_4$, and (d) commercial IrO_2 catalysts within the potential range of 0.926 to 1.526 V vs. RHE at 50 $mV \cdot s^{-1}$ in 1 M KOH electrolyte for TOF analysis.

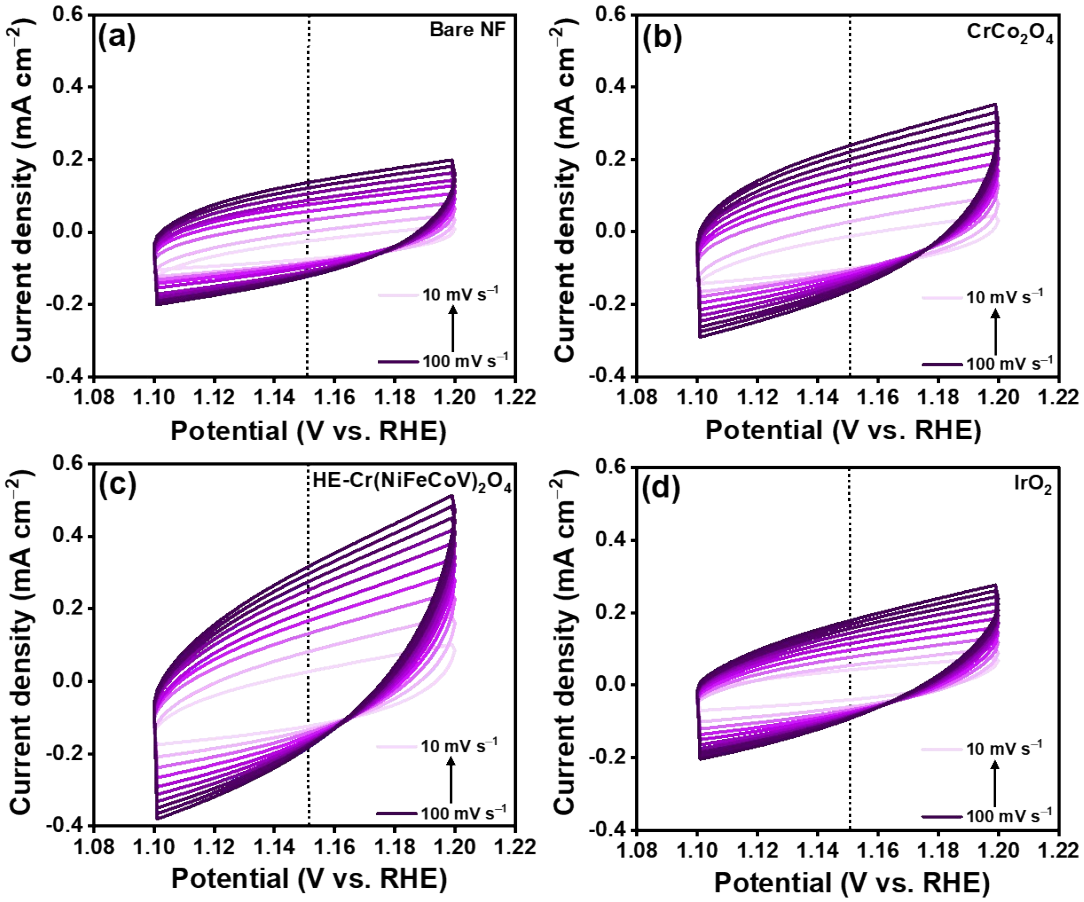

Fig. S11. CV curves of the (a) bare NF, (b) $CrCo_2O_4$, (c) HE-$Cr(NiFeCoV)_2O_4$, and (d) commercial IrO_2 catalysts within the potential range of 1.1 to 1.2 V vs. RHE at 50 $mV \cdot s^{-1}$ in 1 M KOH electrolyte for C_{dl} analysis.

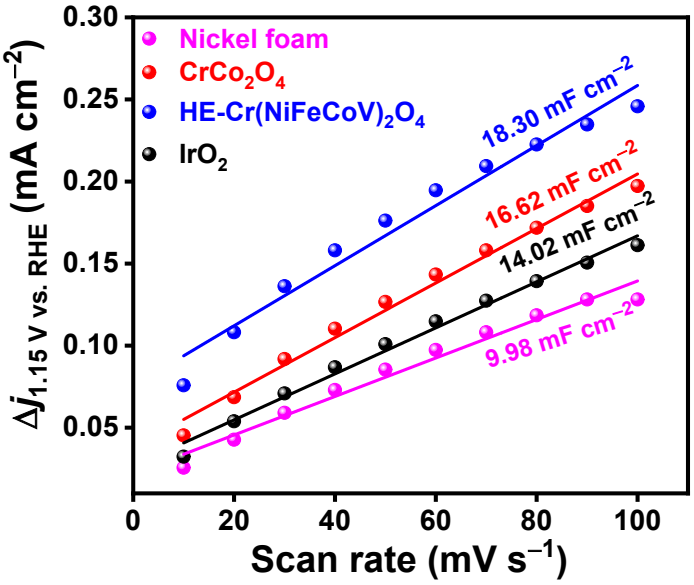

Fig. S12. C_{dl} plots of the bare NF, $CrCo_2O_4$, HE-$Cr(NiFeCoV)_2O_4$, and commercial IrO_2 catalysts.

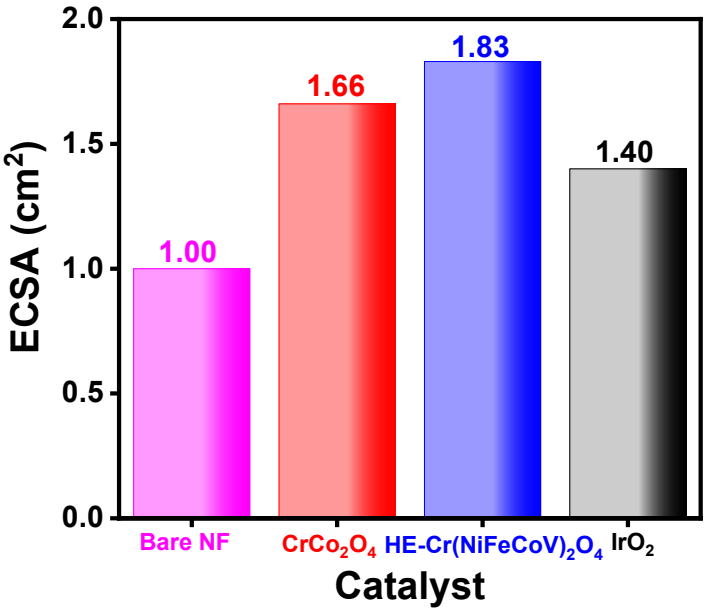

Fig. S13. ECSA values of the bare NF, $CrCo_2O_4$, HE-Cr(NiFeCoV)$_2$O$_4$, and commercial IrO_2 catalysts.

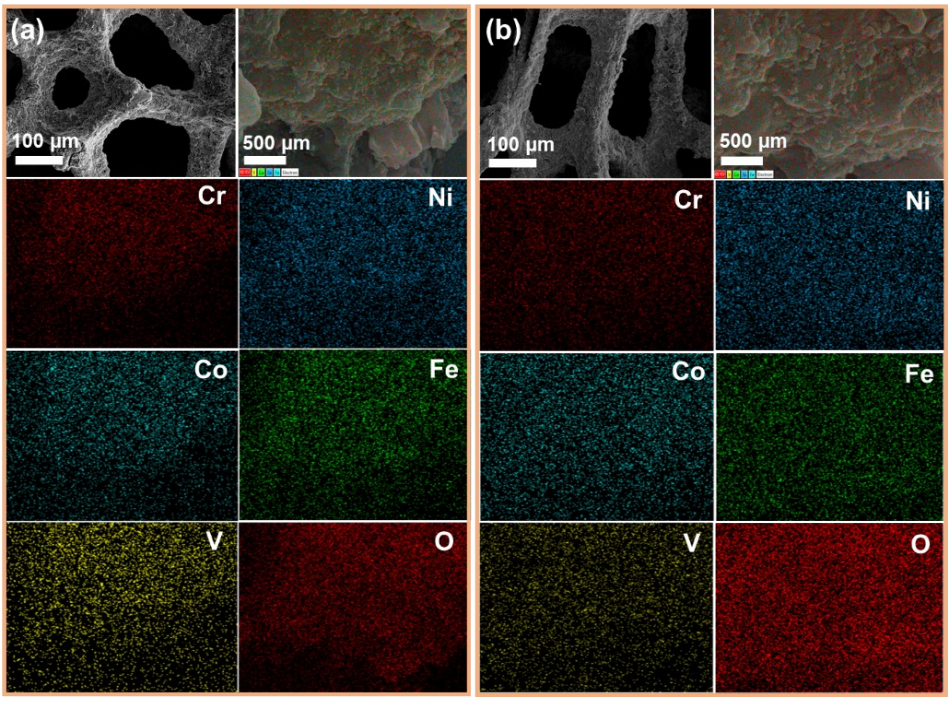

Fig. S14. FE-SEM and EDS mapping images of the HE-Cr$(NiFeCoV)_2O_4$ electrode (a) before and (b) after OER stability test over 100 h.

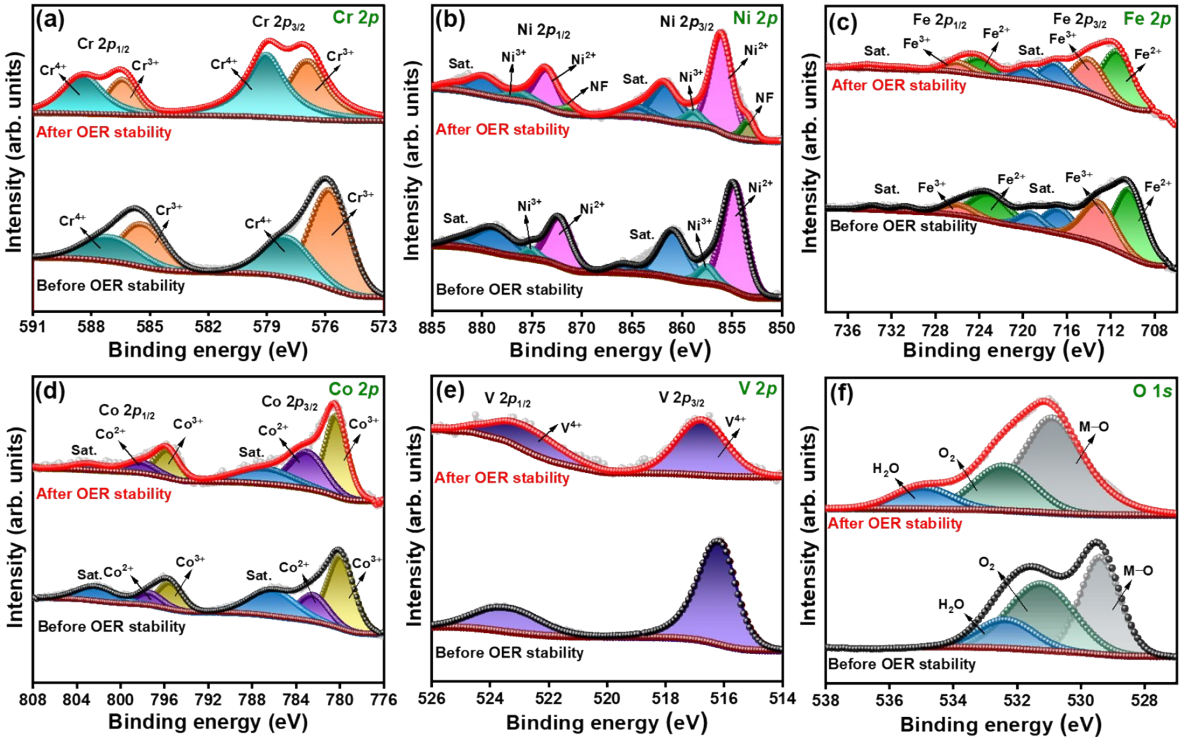

Fig. S15. Core-level XPS spectra of (a) Cr 2*p*, (b) Ni 2*p*, (c) Fe 2*p*, (d) Co 2*p*, (e) V 2*p* and (f) O 1*s* for HE-Cr(NiFeCoV)$_2$O$_4$ electrode before and after OER stability test over 100 h.

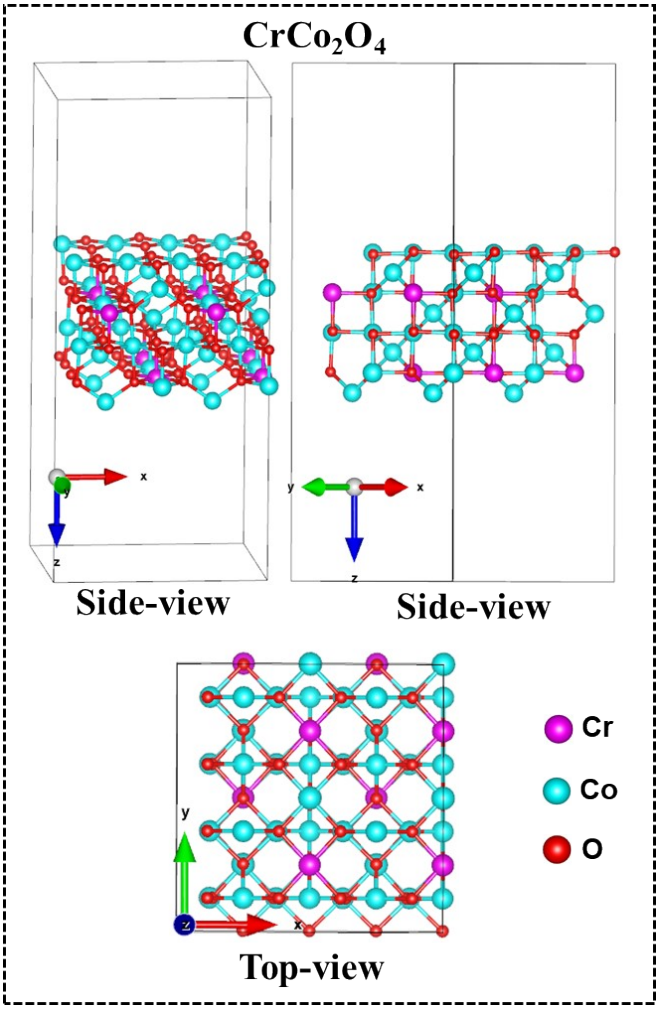

Fig. S16. DFT-derived side-view and top-view crystal structures of the $CrCo_2O_4$ catalyst.

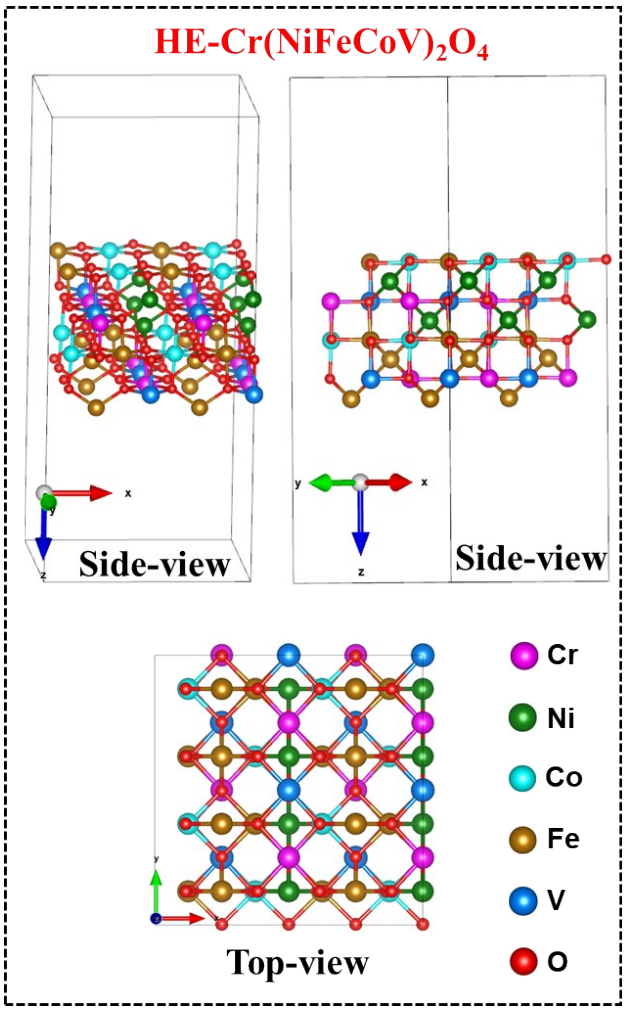

Fig. S17. DFT-derived side-view and top-view crystal structures of the HE-Cr(NiFeCoV)$_2$O$_4$ catalyst.

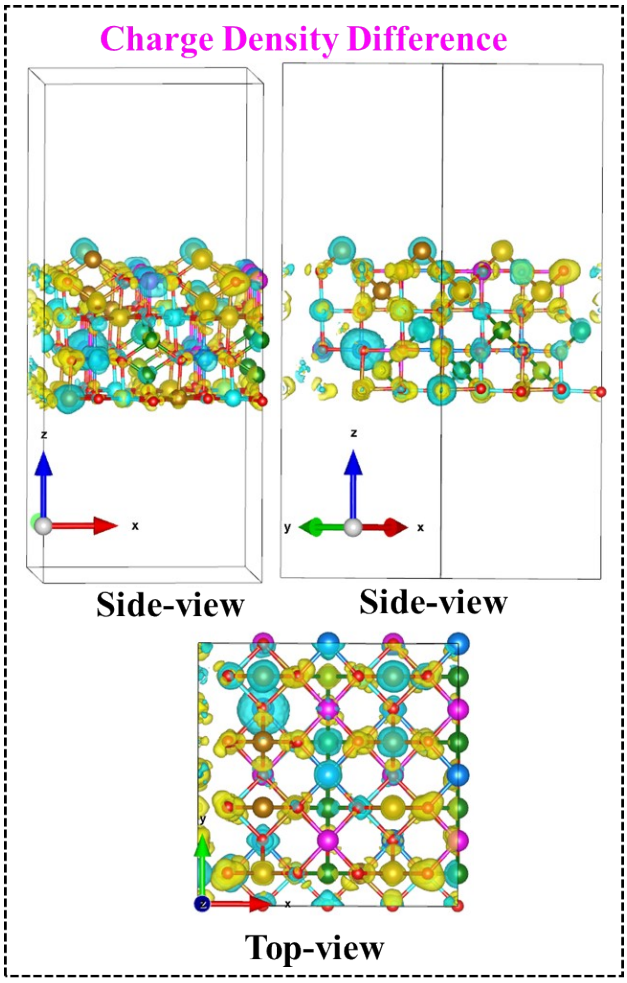

Fig. S18. Charge density difference maps of the HE-Cr$(NiFeCoV)_2O_4$ catalyst showing both side-view and top-view crystal structures.

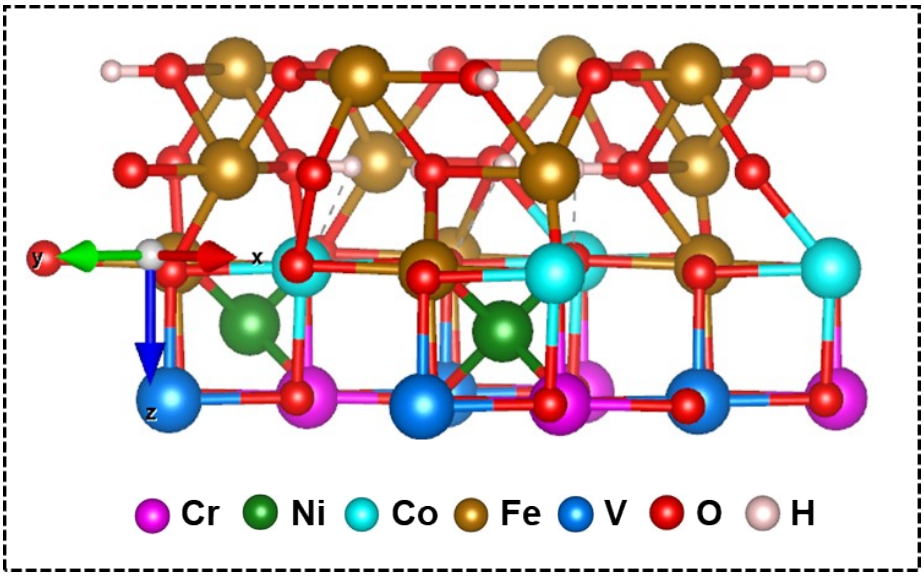

Fig. S19. DFT-predicted crystal structure of surface-formed FeOOH species on the HE-$Cr(NiFeCoV)_2O_4$ catalyst.

Table S1. Comparison of the OER performance of the HE-Cr$(NiFeCoV)_2O_4$ catalyst in terms of overpotentials with previously reported electrocatalysts for OER in 1 M KOH electrolyte.

Electrocatalysts	Overpotential (mV)	Current density (mA cm^{-2})	Reference
HE-Cr$(NiFeCoV)_2O_4$	284	10	**This work**
MnFeCoNiOx	302	10	1
$(CoCuFeMnNi)_3O_4$-MWCNT	350	10	2
$Sr_2Fe_{0.8}Co_{0.2}Mo_{0.6}Co_{0.4}Ox$	345	10	3
FeCoNiCrNbOx core-shell	288	10	4
$K_{0.8}Na_{0.2}(MgMnFeCoNi)F_3$	314	10	5
$(CoCrFeMnNi)_3O_4$	288	10	6
$La(CrMnFeCo_2Ni)O_3$	325	10	7
$(CoNiMnZnFe)_3O_{3.2}$	336	10	8
$(Co_{0.2}Mn_{0.2}Ni_{0.2}Fe_{0.2}Zn_{0.2})Fe_2O_4$	326	10	9
$(Cr_{0.2}Mn_{0.2}Fe_{0.2}Co_{0.2}Ni_{0.2})_3O_4$	350	10	10
$(Mn_{0.2}Fe_{0.2}Ni_{0.2}Mg_{0.2}Zn_{0.2})_3O_4$	293	10	11
$(Cr_{0.2}Mn_{0.2}Fe_{0.2}Ni_{0.2}Zn_{0.2})_3O_4$	295	10	12
$(Cr_{0.2}Mn_{0.2}Fe_{0.2}Co_{0.2}Ni_{0.2})_3O_4$	332	10	13
$Mg_{0.2}Co_{0.2}Ni_{0.2}Cu_{0.2}Zn_{0.2}O$	360	10	14
Fe-NiHF	290	10	15
Dp-$MnCo_2O_4$	327	10	16
CoFeNiCrMn HEO	307	10	17
(MgFeCoNiZn)O	300	10	18
$(NiFeMnCuZn)_3O_4$	308	10	19
NiCo-$(FeCrCoNiAl_{0.1})$Ox	327	10	20
$La_{0.7}Sr_{0.3}Co_{0.2}Mn_{0.2}Ni_{0.2}Fe_{0.2}Al_{0.2}O_3$	339	10	21
HEO/$Ti_3C_2T_x$	331	10	22
NiCoFeMoMn	350	10	23
Co-doped RuO_2 NWs	304	10	24

NiFe-LDH	300	10	25
CoFeLaNiPt HEMG-NP	377	10	26
CoFe-LDH/MXene	319	10	27
NiCoFe-LDH	340	10	28
NiFe-LDH@SWNT	250	10	29
CoNi-LDH@PCPs	350	10	30

Table S2. Comparison of the OWS performance of HE-$Cr(NiFeCoV)_2O_4$ as anode in terms of cell voltages with previously reported OER electrocatalysts for OWS system in 1 M KOH electrolyte.

OER catalyst	Cell voltage	Current density ($mA\ cm^{-2}$)	Reference
$Cr(NiFeCoV)_2O_4$	1.57	10	**This work**
Co/NBC-900	1.68	10	31
Ru-doped Co_3O_4/CoP	1.66	10	32
Mo-Co_3O_4/NC	1.62	10	33
CuO@Cu_3P	1.75	10	34
NP-$NiCo_2O_4$	1.63	10	35
PdZn/TiO_{2-x} NSs	1.67	10	36
Ni-$CoSe_2$/BCT	1.69	10	37
CoO-Co_9S_8/CFP	1.66	10	38
$FeCoS_2$/Co_4S_3/NGF	1.68	10	39
Ni-Mo_xC/NC	1.72	10	40
FeCoSe@NCNSs	1.66	10	41
$NiCo_2Px$/CNTs	1.61	10	42
N-$NiMoO_4$ /NiS_2	1.6	10	43
Co-NC@ Mo_2C	1.68	10	44
Co–P/rGO	1.7	10	45
ONPPGC/OCC	1.66	10	46
Ni_5P_4	1.7	10	47
FeP NTs	1.69	10	48
NiCo-nitrides/$NiCo_2O_4$	1.68	10	49
CoAl–Fe_2N/Fe_3N	1.67	10	50
MoS_2/NiS_2	1.59	10	51
CoP@NC	1.69	10	52
CoP/NCNHP	1.64	10	53
TiN@Ni_3N	1.62	10	54

Co_4Mo_2@NC/Ti	1.74	10	55
W–Co_3S_4@Co_3O_4	1.63	10	56
Co_9S_8-$CoSe_2$	1.66	10	57
NiO/Co_3O_4	1.63	10	58
Co-MnCH	1.68	10	59
$CoMoS_4$	1.72	10	60

References

1. W. Dai, T. Lu and Y. Pan, *Journal of Power Sources*, 2019, **430**, 104-111.
2. D. Wang, Z. Liu, S. Du, Y. Zhang, H. Li, Z. Xiao, W. Chen, R. Chen, Y. Wang and Y. Zou, *Journal of Materials Chemistry A*, 2019, **7**, 24211-24216.
3. H. Sun, X. Xu, G. Chen, Y. Zhou, H. J. Lin, C. T. Chen, R. Ran, W. Zhou and Z. Shao, *ChemSusChem*, 2019, **12**, 5111-5116.
4. Z. Ding, J. Bian, S. Shuang, X. Liu, Y. Hu, C. Sun and Y. Yang, *Advanced Sustainable Systems*, 2020, **4**, 1900105.
5. T. Wang, H. Chen, Z. Yang, J. Liang and S. Dai, *Journal of the American Chemical Society*, 2020, **142**, 4550-4554.
6. C. Duan, X. Li, D. Wang, Z. Wang, H. Sun, R. Zheng and Y. Liu, *Sustainable Energy & Fuels*, 2022, **6**, 1479-1488.
7. T. X. Nguyen, Y. C. Liao, C. C. Lin, Y. H. Su and J. M. Ting, *Advanced Functional Materials*, 2021, **31**, 2101632.
8. Y. Zhang, W. Dai, P. Zhang, T. Lu and Y. Pan, *Journal of Alloys and Compounds*, 2021, **868**, 159064.

9. Y. Zhang, T. Lu, Y. Ye, W. Dai, Y. a. Zhu and Y. Pan, *ACS Applied Materials & Interfaces*, 2020, **12**, 32548-32555.

10. M. Einert, M. Mellin, N. Bahadorani, C. Dietz, S. Lauterbach and J. P. Hofmann, *ACS Applied Energy Materials*, 2022, **5**, 717-730.

11. D. Stenzel, B. Zhou, C. Okafor, M. V. Kante, L. Lin, G. Melinte, T. Bergfeldt, M. Botros, H. Hahn and B. Breitung, *Frontiers in Energy Research*, 2022, **10**, 942314.

12. X. Yang, S. Liping, L. Qiang, H. Lihua and Z. Hui, *Journal of Materials Chemistry A*, 2022, **10**, 17633-17641.

13. Z. Sun, Y. Zhao, C. Sun, Q. Ni, C. Wang and H. Jin, *Chemical Engineering Journal*, 2022, **431**, 133448.

14. F. Liu, M. Yu, X. Chen, J. Li, H. Liu and F. Cheng, *Chinese Journal of Catalysis*, 2022, **43**, 122-129.

15. T. Wang, Y. Wu, Y. Han, P. Xu, Y. Pang, X. Feng, H. Yang, W. Ji and T. Cheng, *ACS Applied Nano Materials*, 2021, **4**, 14161-14168.

16. K. Lankauf, K. Cysewska, J. Karczewski, A. Mielewczyk-Gryń, K. Górnicka, G. Cempura, M. Chen, P. Jasiński and S. Molin, *International Journal of Hydrogen Energy*, 2020, **45**, 14867-14879.

17. J. Baek, M. D. Hossain, P. Mukherjee, J. Lee, K. T. Winther, J. Leem, Y. Jiang, W. C. Chueh, M. Bajdich and X. Zheng, *Nature Communications*, 2023, **14**, 5936.

18. H. Wu, Q. Lu, Y. Li, J. Wang, Y. Li, R. Jiang, J. Zhang, X. Zheng, X. Han and N. Zhao, *Nano Letters*, 2022, **22**, 6492-6500.

19. P. Edalati, Q. Wang, H. Razavi-Khosroshahi, M. Fuji, T. Ishihara and K. Edalati, *Journal of Materials Chemistry A*, 2020, **8**, 3814-3821.

20. S. Zhao, H. Wu, R. Yin, X. Wang, H. Zhong, Q. Fu, W. Wan, T. Cheng, Y. Shi and G. Cai, *Journal of Alloys and Compounds*, 2021, **868**, 159108.

21. H. Wu, Q. Lu, Y. Li, M. Zhao, J. Wang, Y. Li, J. Zhang, X. Zheng, X. Han and N. Zhao, *Journal of the American Chemical Society*, 2022, **145**, 1924-1935.

22. C. E. Park, R. A. Senthil, G. H. Jeong and M. Y. Choi, *Small*, 2023, **19**, 2207820.

23. H. Liu, H. Qin, J. Kang, L. Ma, G. Chen, Q. Huang, Z. Zhang, E. Liu, H. Lu and J. Li, *Chemical Engineering Journal*, 2022, **435**, 134898.

24. J. Wang, Y. Ji, R. Yin, Y. Li, Q. Shao and X. Huang, *Journal of Materials Chemistry A*, 2019, **7**, 6411-6416.

25. F. Song and X. Hu, *Nature communications*, 2014, **5**, 4477.

26. M. W. Glasscott, A. D. Pendergast, S. Goines, A. R. Bishop, A. T. Hoang, C. Renault and J. E. Dick, *Nature communications*, 2019, **10**, 2650.

27. C. Hao, Y. Wu, Y. An, B. Cui, J. Lin, X. Li, D. Wang, M. Jiang, Z. Cheng and S. Hu, *Materials Today Energy*, 2019, **12**, 453-462.

28. L. Qian, Z. Lu, T. Xu, X. Wu, Y. Tian, Y. Li, Z. Huo, X. Sun and X. Duan, *Advanced Energy Materials*, 2015, **5**, 1500245.

29. H. Liu, J. Zhou, C. Wu, C. Wang, Y. Zhang, D. Liu, Y. Lin, H. Jiang and L. Song, *ACS Sustainable Chemistry & Engineering*, 2018, **6**, 2911-2915.

30. W. Wang, Y. Lu, M. Zhao, R. Luo, Y. Yang, T. Peng, H. Yan, X. Liu and Y. Luo, *ACS Nano*, 2019, **13**, 12206-12218.

31. M. R. Liu, Q. L. Hong, Q. H. Li, Y. Du, H. X. Zhang, S. Chen, T. Zhou and J. Zhang, *Advanced Functional Materials*, 2018, **28**, 1801136.

32. K. Zhang, W. Ma, G. Tan, Z. Cheng, Y. Ma, W. Li, X. Feng and Z. Li, *Molecular Catalysis*, 2022, **530**, 112640.

33. X. Zhao, F. Yin, X. He, B. Chen and G. Li, *International Journal of Hydrogen Energy*, 2021, **46**, 20905-20918.

34. S. Lv, J. Li, B. Zhang, Y. Shi, X. Liu and T. Wang, *International Journal of Hydrogen Energy*, 2022, **47**, 9593-9605.

35. R. Elakkiya, R. Ramkumar and G. Maduraiveeran, *Materials Research Bulletin*, 2019, **116**, 98-105.

36. K. M. Naik, K. Hashisake, E. Higuchi and H. Inoue, *Materials Advances*, 2023, **4**, 561-569.

37. G. Yang, Y. Zhang, J. Liu, M. Wang, C. Gu and J. Li, *International Journal of Hydrogen Energy*, 2022, **47**, 38920-38929.

38. X. Chen, R. Jiang, C. Dong, H. Liu, J. Yang and X. Du, *ChemElectroChem*, 2022, **9**, e202101566.

39. S. Wang, X. He, S. Wang, X. Huang, M. Wu and D. Xiang, *Electrochimica Acta*, 2023, **441**, 141790.

40. D. Das, S. Santra and K. K. Nanda, *ACS Applied Materials & Interfaces*, 2018, **10**, 35025-35038.

41. Y. Pan, M. Wang, M. Li, G. Sun, Y. Chen, Y. Liu, W. Zhu and B. Wang, *Journal of Energy Chemistry*, 2022, **68**, 699-708.

42. C. Huang, T. Ouyang, Y. Zou, N. Li and Z.-Q. Liu, *Journal of Materials Chemistry A*, 2018, **6**, 7420-7427.

43. L. An, J. Feng, Y. Zhang, R. Wang, H. Liu, G. C. Wang, F. Cheng and P. Xi, *Advanced Functional Materials*, 2019, **29**, 1805298.

44. Q. Liang, H. Jin, Z. Wang, Y. Xiong, S. Yuan, X. Zeng, D. He and S. Mu, *Nano Energy*, 2019, **57**, 746-752.

45. L. Jiao, Y.-X. Zhou and H.-L. Jiang, *Chemical Science*, 2016, **7**, 1690-1695.

46. J. Lai, S. Li, F. Wu, M. Saqib, R. Luque and G. Xu, *Energy & Environmental Science*, 2016, **9**, 1210-1214.

47. M. Ledendecker, S. Krick Calderón, C. Papp, H. P. Steinrück, M. Antonietti and M. Shalom, *Angewandte Chemie International Edition*, 2015, **54**, 12361-12365.

48. Y. Yan, B. Y. Xia, X. Ge, Z. Liu, A. Fisher and X. Wang, *Chemistry–A European Journal*, 2015, **21**, 18062-18067.

49. Z. Liu, H. Tan, D. Liu, X. Liu, J. Xin, J. Xie, M. Zhao, L. Song, L. Dai and H. Liu, *Advanced Science*, 2019, **6**, 1801829.

50. B. H. R. Suryanto, Y. Wang, R. K. Hocking, W. Adamson and C. Zhao, *Nature Communications*, 2019, **10**, 5599.

51. J. Lin, P. Wang, H. Wang, C. Li, X. Si, J. Qi, J. Cao, Z. Zhong, W. Fei and J. Feng, *Advanced Science*, 2019, **6**, 1900246.

52. Z. Li, J. Sui, Q. Zhang, J. Yu, L. Yu and L. Dong, *International Journal of Hydrogen Energy*, 2021, **46**, 2095-2102.

53. Z. Li, H. Feng, M. Song, C. He, W. Zhuang and L. Tian, *Materials Today Energy*, 2021, **20**, 100698.

54. Q. Zhang, Y. Wang, Y. Wang, A. M. Al-Enizi, A. A. Elzatahry and G. Zheng, *Journal of Materials Chemistry A*, 2016, **4**, 5713-5718.

55. J. Jiang, Q. Liu, C. Zeng and L. Ai, *Journal of Materials Chemistry A*, 2017, **5**, 16929-16935.

56. C. Wang, X. Du and X. Zhang, *International Journal of Hydrogen Energy*, 2023, **48**, 12739-12752.

57. S. Chakrabartty, S. Karmakar and C. R. Raj, *ACS Applied Nano Materials*, 2020, **3**, 11326-11334.

58. X. Wei, Y. Zhang, H. He, D. Gao, J. Hu, H. Peng, L. Peng, S. Xiao and P. Xiao, *Chemical Communications*, 2019, **55**, 6515-6518.

59. T. Tang, W.-J. Jiang, S. Niu, N. Liu, H. Luo, Y.-Y. Chen, S.-F. Jin, F. Gao, L.-J. Wan and J.-S. Hu, *Journal of the American Chemical Society*, 2017, **139**, 8320-8328.

60. Y. Sun, C. Wang, T. Ding, J. Zuo and Q. Yang, *Nanoscale*, 2016, **8**, 18887-18892.